A synergistic integration of photogrammetry and Gaussian Splatting for back-in-time quality inspection

Italian Manufacturing Association Conference - XVII AITeM Materials Research Forum LLC
Materials Research Proceedings 57 (2025) 20-28 https://doi.org/10.21741/9781644903735-3

A synergistic integration of photogrammetry and Gaussian Splatting for back-in-time quality inspection

Mattia TROMBINI[1,a*], Domenico A. MAISANO[1,b*], Fiorenzo FRANCESCHINI[1,c*]

[1]Department of Management and Production Engineering (DIGEP), Politecnico di Torino, 10129 Torino, Italy

[a]mattia.trombini@polito.it, [b]domenico.maisano@polito.it, [c]fiorenzo.franceschini@polito.it

Keywords: Inspection, Quality, Back-in-Time Repeatability

Abstract. Photogrammetry is a well-established technique for 3D inspection of manufactured objects and machinery but its static nature limits re-inspection. If images lead to poor reconstruction, e.g., due to insufficient coverage, the object's original state may become inaccessible, preventing further analysis. This work introduces a synergistic integration of photogrammetry and Gaussian Splatting (GS) to enable *back-in-time* quality inspection. GS creates "frozen" and fully navigable 3D digital scenes, i.e., high-fidelity 3D representations encoded with Gaussians, that preserve the spatial and temporal state of the object at the time of acquisition, allowing the generation of novel synthetic views (i.e., renders) to enrich the original photogrammetric reconstruction. A preliminary case study on the inlet lip skin part of the engine of an aircraft demonstrates how GS renders, when integrated into the photogrammetric workflow, improve the characterisation of surface defects. Results show enhanced defect localisation and a clearer delineation of damage geometry, suggesting that the proposed integration enables effective *back-in-time* inspections.

Introduction

Ensuring the quality and integrity of manufactured goods and industrial machinery requires accurate inspection techniques. Traditional methods often rely on non-destructive testing (NDT) [1], but advances in visual analysis have led to the increasing use of photogrammetry [2]. This technique enables high-fidelity spatial data acquisition, providing a detailed geometric assessment of objects. The integration with unmanned aerial vehicles (UAVs) [3] may further enhance inspection capabilities, facilitating multi-perspective analysis, frequent assessments and reducing health risks for inspectors, particularly in Large-Scale Dimensional Metrology (LSDM) [4,5]. While photogrammetry offers significant advantages, its static nature imposes significant limitations on re-inspection. If the image coverage is inadequate, the reconstruction cannot be subsequently improved by acquiring additional images, since (i) the object may no longer be available for new acquisitions due to service re-entry, even in remote locations, and (ii) external factors such as mechanical vibration or thermal effects may have changed the state of the object in analysis. Even in the absence of significant changes, each subsequent image can show the component in a slightly different state, making direct comparisons between states difficult and limiting the ability to trace the initiation of possible defects. Furthermore, if a defect is discovered in a subsequent inspection, there is no way to retrospectively verify whether it was already present but previously undetected, as past reconstructions are limited by the constraints of the images originally captured. While it is possible to re-examine the object, new viewing perspectives cannot be introduced, and no finer detail can be retrieved beyond the resolution and frame of the original acquisition.

A potential solution to this complex problem can be found in the concept of 3D scene [6], which is a comprehensive, high-fidelity digital representation of an object or environment at a given moment in time. A 3D scene captures not only the geometry of the object, which defines its shape and structure, but also enhances the realism with additional elements. Specifically, textures are employed to provide surface details such as colours and patterns, lighting is utilised to simulate light sources, thereby creating shadows, highlights and depth, whereas camera perspective is determined to visualise the scene [7]. The high level of realism afforded by a 3D scene facilitates the re-exploration of objects in their original condition, thereby enabling the generation of novel viewpoints and perspectives that would otherwise be inaccessible, facilitating retrospective analysis and permitting detailed inspections beyond the constraints of the initial acquisition.

The emergence of Neural Radiance Field (NeRF) [8] represented a breakthrough, introducing the concepts of sampling and positional encoding to enhance rendering quality. However, despite the notable advancements in rendering quality, the training and rendering times remain extremely high, often exceeding 40 hours using 4-GPU A100 [9]. The recent introduction of 3D Gaussian Splatting (GS) [9] offers a novel approach to efficiently creating a 3D scene, overcoming the limitations of NeRF, with training times reduced to approximately 30 minutes on an A6000 GPU [9]. GS employs a set of Gaussian ellipsoids to model the scene, enabling efficient rendering by rasterising these ellipsoids into images. Further details concerning the technique are discussed in literature [9] and briefly mentioned throughout this paper.

The research question addressed in this study concerns the integration of *back-in-time* visual analysis with high-fidelity 3D scene representation, specifically using Gaussian Splatting, to investigate unexpected defects observed during an inspection. A defect may have either gone completely unnoticed in previous inspections or may have been observed but without a clear definition of its full extent. By revisiting past states, it is possible to more accurately evaluate whether the defect was already present but undetected or insufficiently defined in terms of contour and extent. By employing Gaussian Splatting, this approach seeks to enhance quality in photogrammetric point clouds, exploiting the combination of real images with virtual renders, thus improving reconstruction density and defect detection in terms of quantity, clarity, and dimensional accuracy. It is important to underline that the reconstruction of the 3D scene does not require the acquisition of additional images. Instead, images belonging to a specific past state of the object can be used to generate the scene. The overarching objective of this research is to establish a framework for integrating 3D scene rendering with photogrammetry, ultimately advancing inspection methodologies in manufacturing and industrial settings.

The paper includes an overview of typical defect types in the aerospace sector, followed by a brief explanation of the fundamentals of both photogrammetry and Gaussian Splatting. A case study on the inlet lip skin part of the engine of an aircraft is then presented to demonstrate the proposed synergy and the final section draws some preliminary conclusions.

Taxonomy of defects in manufacturing contexts

In accordance with the aeronautical test case further discussed throughout this paper, the current section aims to provide an overview of typical defects that may affect the operability of objects and that recurrent inspection activities seek to detect. The aeronautical sector is a highly regulated and technologically advanced industry that prioritises safety, efficiency, and durability in aircraft design and maintenance [10]. Aircraft components are subjected to extreme conditions, including high aerodynamic loads, temperature fluctuations, and corrosion-prone environments [11]. Consequently, rigorous inspection and maintenance protocols are implemented to detect and mitigate structural defects before they may escalate into critical failures. These defects include:

- Defects in metallic materials;
- Defects in composite materials;
- Defects in coatings;
- Defects in joints.

Materials Research Proceedings 57 (2025) 20-28 https://doi.org/10.21741/9781644903735-3

The present study focuses on metallic components, particularly defects that arise during in-service conditions, which are characterised by their unpredictability, making it challenging to foresee and diagnose. If undetected, such damage can compromise structural integrity, potentially leading to catastrophic consequences. The categorisation presented in Table 1 is proposed for the establishment of a comprehensive taxonomy of defects and the evaluation of their detectability through photogrammetric inspection. Creep has been excluded from this classification, since elevated temperatures are not typically encountered in standard inspections of aerospace structures, making creep-related deformation not appropriate to the scope of this study [11].

Table 1. *Categorisation of defect types and expected detectability using Machine Vision systems in the aerospace industry [11].*

Type	Description	Classification	Detectable
Fatigue	Degradation and final failure of the materials under cyclic loads, which intensity is always lower than the tensile strength of the material.	Cracks	Partially*
		Surface discoloration / deformation	Yes
		Internal failure	No
Corrosion	Deterioration of the material due to chemical reaction with the environment.	Rust/oxide layer	Yes
		Pitting	Yes
		Subsurface defects	No
Operational overload	Fracture of the component when exceeding the design stress of a material, e.g., damage due to bird strike and landing gear failure after hard landings.	Fracture	Partially*
		Plastic deformation	Partially*
		Internal fracture	No
Wear	Deterioration of the material due to mechanical action that gradually reduces life cycle.	Scratch/grooves	Yes
		Deviation of material thickness	Partially**
Extreme weather conditions	Damage that occurs due to climate conditions, including ice and lightning impacts.	Surface degradation	Yes
		Material discoloration / texture changes	Yes
		Micro-cracking	No
Welding	Defects that may occur in the areas of welded joints.	Porosity/cracks	Partially**
		Misalignment	Yes
		Incomplete fusion	No
		Residual stress	No

*only if on surface
**detectability depends on defect size and on photogrammetric accuracy

Fundamentals of photogrammetry

Photogrammetry involves the use of an array of cameras strategically positioned within a defined measurement area to accurately identify distinct visual features. The photogrammetric process can involve different image capturing modalities, considering (i) multiple cameras able to collect images simultaneously, (ii) a single camera moving around the fixed scene, and (iii) a single fixed camera with a moving object on a rotating turntable [12]. In this study, a camera mounted as a payload on a drone is used and the camera pose network is generated by capturing frames from multiple positions during flight, holding the scene fixed and deploying a moving camera. The captured data is processed by an external Data Processing Unit (DPU), enabling either wireless or cable-based connectivity. As illustrated in Fig. 1, the 3D coordinates of an optical marker, denoted as M_j, are connected to the 2D coordinates of the corresponding image point, $P_{i,j}$, on the projection plane of the i-th camera.

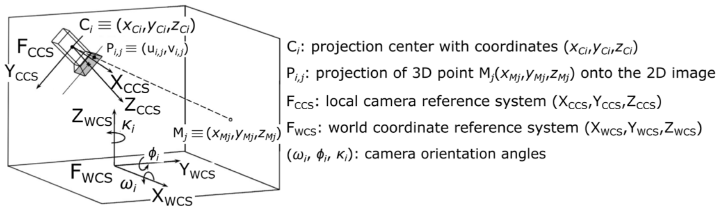

Fig. 1. *Generic setup of a single camera-based localisation in 3D space (adapted from [12]).*

The process is executed through the application of collinearity equations using homogeneous coordinates [2,13], summarised in Eq. (1).

$$\lambda_i \times \begin{bmatrix} u_{i,j} \\ v_{i,j} \\ 1 \end{bmatrix} = \mathbf{K}_i \times \mathbf{W}_i \times \begin{bmatrix} x_{M_j} \\ y_{M_j} \\ z_{M_j} \\ 1 \end{bmatrix} = \begin{bmatrix} u_{f_i} & 0 & u_{0_i} & 0 \\ 0 & v_{f_i} & v_{0_i} & 0 \\ 0 & 0 & 1 & 0 \end{bmatrix} \times \begin{bmatrix} \mathbf{R}_i & -\mathrm{C}_i \\ 0 & 1 \end{bmatrix} \times \begin{bmatrix} x_{M_j} \\ y_{M_j} \\ z_{M_j} \\ 1 \end{bmatrix} \tag{1}$$

where λ_i denotes a non-zero scale factor, and $\mathbf{K}_i$ is the 3x4 intrinsic parameter matrix, composed by u_{0i} and v_{0i} representing the coordinates of the image centre, while u_{fi} and v_{fi} correspond to the focal length components related to the camera. $\mathbf{W}_i$ is the 4x4 matrix representing the external parameters, with $\mathbf{R}_i$ (ω_i, ϕ_i, κ_i) defined as the rotations matrix, defining the relationship between the world coordinate reference system (F_{WCS}) and the local camera coordinate system (F_{CCS}). C_i is the term related to the projection centre in the local camera coordinate system F_{CCS}. Commonly, it is defined $\mathbf{P}_i = \mathbf{K}_i \times \mathbf{W}_i$ as the camera projection matrix. In order to address lens distortions, correction factors are incorporated in the collinearity equation, accounting for radial, tangential, and skew distortions, as detailed in Eq. (2):

$$\lambda_i \times \begin{bmatrix} \tilde{u}_{i,j} \\ \tilde{v}_{i,j} \\ 1 \end{bmatrix} = \lambda_i \times \begin{bmatrix} 1 & 0 & \delta u_{R_{i,j}} + \delta u_{T_{i,j}} + \delta u_{S_{i,j}} \\ 0 & 1 & \delta v_{R_{i,j}} + \delta v_{T_{i,j}} \\ 0 & 0 & 1 \end{bmatrix} \times \begin{bmatrix} u_{i,j} \\ v_{i,j} \\ 1 \end{bmatrix} = \mathbf{P}_i \times \begin{bmatrix} x_{M_j} \\ y_{M_j} \\ z_{M_j} \\ 1 \end{bmatrix} \tag{2}$$

where $\delta u_{Ri,j}$ and $\delta v_{Ri,j}$ account for the radial distortion, $\delta u_{Ti,j}$ and $\delta v_{Ti,j}$ represent the tangential distortion and, eventually, $\delta u_{Si,j}$ is the skewness-related term [12,14]. Photogrammetric reconstruction generates a point cloud as output, consisting of 3D points defined by their coordinates within a spatial reference frame, with each point representing a part of the object's surface [11].

Gaussian Splatting methodology

Gaussian Splatting methodology offers a significant departure from traditional methods like NeRF [9], being a state-of-the-art technique for representing and rendering 3D scenes. This approach prioritises computational efficiency, interpretability, and high-quality visual output, addressing several limitations inherent in NeRF and other neural representations [8]. GS represents a scene as a collection of 3D Gaussian ellipsoids. Each ellipsoid is characterised by the following parameters:

- *Position*: corresponding to its centre point, identifying the spatial location.
- *Covariance matrix:* defining the orientation, size, and shape of the ellipsoid in space.
- *Colour and opacity*: governing the visual appearance and blending behaviour.

GS is a process of rendering that involves the projection of 3D Gaussian ellipsoids onto a 2D image plane to produce a final rendering image. The core of this process is rasterisation, whereby the 3D ellipsoids are directly mapped to 2D pixels on the image plane. Gradient descent techniques play a fundamental role in tuning the abovementioned parameters [9], e.g., position and colour, thereby ensuring an accurate representation of the scene's geometry and appearance.

Materials Research Proceedings 57 (2025) 20-28 https://doi.org/10.21741/9781644903735-3

Instrumentation
In this study, the object of interest is an inlet lip skin part of the engine of an aircraft (see Fig. 2 for reference). The object has an external diameter of approximately 1200 mm and has been transported and installed in a designated location at the Politecnico di Torino, which is suitable for drone operations. The selection of this artefact is driven by the objective of the study, which necessitates the presence of an object of relatively large dimensions, exhibiting a discernible defect. A portion of the surface shows visible damage defined as a bump consistent with the impact caused by the collision with a flock of birds, categorising the defect as an operational overload (bird strike [15]). Images of the component are captured using a Matrice 350RTK drone equipped with a Zenmuse L2 camera and processed by Metashape© [16] for generating photogrammetric reconstructions. Gaussian Splatting is entirely code-based in Python using the PyTorch framework and custom CUDA© for rasterisation, with a completion time of about 35 minutes.

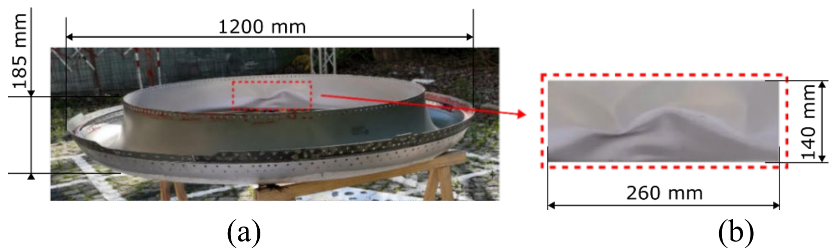

Fig. 2. *(a) Real images of the inlet lip skin part of an engine of an aircraft used as a case study for demonstrating the combination of photogrammetry and Gaussian Splatting, and (b) detail of the bump shape. The image provides also the approximate overall dimensions.*

Preliminary results

In this section, a preliminary case study is analysed in order to facilitate a more comprehensive evaluation of the capabilities of combining photogrammetry and Gaussian Splatting. This combination aims to delineate the discrepancies that may emerge during the inspection of a damaged area when input is augmented with localised renders in the proximity of the defect. The object under consideration is the inlet lip skin in Fig. 2 and two different photogrammetric configurations are analysed:

- Case A, consisting of 200 real images;
- Case B, consisting of 200 real images augmented with 30 novel GS renders.

The collection of 200 real images serves as a reference for the Gaussian Splatting pipeline and the generation of the 3D scene. In the generation of case B, 30 additional images, extracted from the 3D GS scene, are obtained from entirely novel viewpoints aiming to enrich the defect visualisation. Consequently, there is no correspondence between reference images and new renders, since the observation angles and location are by definition novel.

To compute the differences between the clouds, it is fundamental to create a reference surface fitting the internal toroidal surface of the lip. The RANdom SAmple Consensus (RANSAC) [17] fitting toroidal surface is created using the undamaged portion of the surface as a reference, with the point clouds then being overlaid onto the theoretical surface corresponding to this undamaged portion. This approach enables the computation of cloud-to-surface distances, highlighting any differences between the point clouds. As illustrated in Figs. 3a and 3b, each point cloud is projected from 3D onto the 2D image plane where the image of the bump lies. This projection enables the points to be superimposed onto the image, creating a density map where the colour represents the computed distances. The map provides a clear visualisation of variations between the theoretical and observed surfaces. Finally, Table 2 is used to define parameters for comparing the point clouds. The “Average 1” column corresponds to the average distance values when considering the overall extent of the map. The “Average 2” column represents the average distance excluding values close to 0 mm, since areas where the distance is 0 indicate the absence of defect. This allows a specific comparison of only the regions where the bump is extended. The "Coverage" column assesses the percentage of the surface affected by damage, defined as the ratio between the portion of the surface characterised by a distance from the reference surface lower than 0 mm and the total surface area. In addition, the remaining columns provide a detailed comparison of specific points of interest. For clarity, distances are shown with negative values since the bump in the damaged area brings the object's surface closer to the centre of the fitting toroid than in the undamaged area. "Peak 1" corresponds to the negative peak of distance in case A (labelled as A1 in the figure), and its value in case B is evaluated at the same coordinates (labelled as B1). Similarly, "Peak 2" and "Peak 3" represent the two minima in case B (labelled as B2 and B3, respectively), and their values in case A are evaluated at the same coordinates (labelled as A2 and A3). As illustrated in Fig. 4, in the context of case B, the measurements B1, B2, and B3 are assigned a negative sign, as they denote distances measured inward relative to the mean surface of the toroid, according to the local reference frame. An equivalent consideration applies to case A.

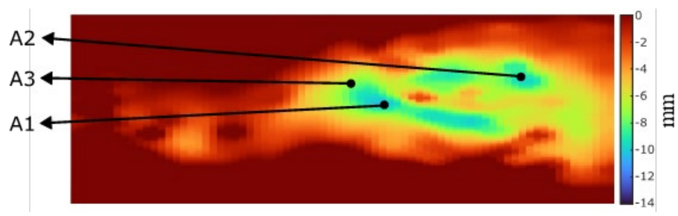

(a) Case A

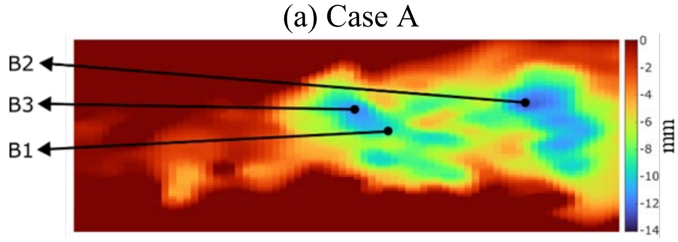

(b) Case B

Fig. 3. *Projection of point cloud and colour density map based on the distance from best fitting primitive in the damaged area considering (a) case A and (b) case B. Point A1 corresponds to the negative peak of distance in case A, and its counterpart in case B is evaluated at the same coordinates (labelled as B1). B2 and B3 represent two local minima in case B, and their corresponding values in case A are evaluated at the same coordinates (labelled as A2 and A3).*

By observing these results, some preliminary comments can be proposed:

- Case B demonstrates a higher level of damage, as demonstrated in Table 2. Furthermore, "Peak 1" demonstrates consistency across both cases, with a value of -10.05 mm for case A and -10.34 mm for case B. Conversely, case B permits the identification of a greater number of minima, which are less pronounced in case A (see Fig. 3 for reference).
- The cloud in case A is composed of 1994 points, while case B consists of 2071 points. The difference in points is negligible, but the *back-in-time* paradigm is clearly demonstrated. The initial photogrammetric reconstruction, created using 200 real images, provides an approximate geometry of the defect, with its shape and extent significantly underestimated. In contrast, re-examining the object's state at the time of initial acquisition within the 3D scene allows for more precise delineation of the bump geometry in contours and distance peaks from the average reference surface.

Table 2. *Comparison between case A (real images) and case B (real images + GS renders) based on peak distances from the best-fit primitive, along with an evaluation of the damaged area extent.*

	Average 1 / [mm]	Average 2 / [mm]	Coverage / -	Peak 1 / [mm]	Peak 2 / [mm]	Peak 3 / [mm]
Case A	-2.48	-4.23	59%	A1: -10.05	A2: -9.49	A3: -7.03
Case B	-3.46	-5.14	67%	B1: -10.34	B2: -11.83	B3: -11.30

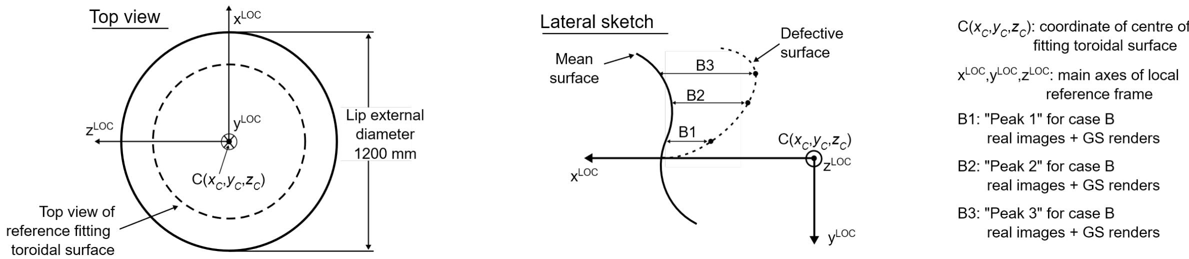

Fig. 4. *Top and sketch view of the inlet lip skin. Definition of the distances B1, B2, B3 relative to the mean surface of the fitting toroid. The measurements are assigned a negative sign as they represent displacements inward with respect to the reference mean surface. The same logic applies to points A1, A2 and A3 (case A), although they are not shown in the figure to avoid overloading the visual representation.*

Conclusions

This work preliminarily explored the integration of photogrammetry and Gaussian Splatting as a novel approach to enhance quality inspection through the novel concept of *back-in-time* analysis. By generating “frozen” and fully navigable 3D scenes from the original image acquisitions, GS enables the extraction of synthetic views (i.e., renders) from previously inaccessible perspectives, without requiring new physical acquisitions. Renders can be introduced into the photogrammetric workflow, along with real images, improving point cloud density and the accuracy of defect characterisation. Once integrated into the photogrammetric pipeline, renders enrich the original acquisitions while preserving the same temporal state, thus enabling retrospective inspection. GS introduces the innovative paradigm of *back-in-time repeatability* into photogrammetry by enabling multiple analyses of the same object state, corresponding to a specific moment in time, regardless of the current condition or availability of the physical asset.

The preliminary case study confirmed the potential of this approach to detect and refine the geometry of surface damage, particularly in areas that were insufficiently covered during initial acquisition. The increased spatial coverage and the ability to revisit the exact temporal state of an object represent a meaningful advancement over conventional inspection techniques.

Beyond the specific application presented, the proposed synergy introduces the concept of *back-in-time repeatability* into the field of 3D reconstruction, expanding photogrammetry from a static imaging tool to a dynamic spatio-temporal framework. This paradigm shift opens novel possibilities in industrial inspection, product traceability, lifecycle monitoring, and digital asset management.

Future research will focus on validating this approach across different defect types (e.g., corrosion, wear), refining integration protocols, and assessing its scalability for real-world industrial environments.

Acknowledgements
This study was carried out within the Space It Up project funded by the Italian Space Agency, ASI, and the Ministry of University and Research, MUR, under contract n. 2024-5-E.0 - CUP n. I53D24000060005.

References

[1] Garnier C, Pastor M-L, Eyma F, Lorrain B (2011) The detection of aeronautical defects in situ on composite structures using Non Destructive Testing. Composite Structures 93(5):1328-1336. https://doi.org/10.1016/j.compstruct.2010.10.017

[2] Mikhail EM, Bethel JS, Mcglone JC (2001) Introduction to Modern Photogrammetry. 1st edn. John Wiley & Sons, New York, USA.

[3] Colomina I, Molina P (2014) Unmanned aerial systems for photogrammetry and remote sensing: A review. ISPRS Journal of Photogrammetry and Remote Sensing 92:79-97. https://doi.org/10.1016/j.isprsjprs.2014.02.013

[4] Franceschini F, Galetto M, Maisano D, Mastrogiacomo L, Pralio B (2011) Distributed Large-Scale Dimensional Metrology: New Insights. 1st edn. Springer London. https://doi.org/10.1007/978-0-85729-543-9_1

[5] Franceschini F, Galetto M, Maisano D, and Mastrogiacomo L (2015) Combining multiple Large Volume Metrology systems: Competitive versus cooperative data fusion. Precision Engineering 43:514-524. https://doi.org/10.1016/j.precisioneng.2015.09.014

[6] Sitzmann V, Zollhöfer M, and Wetzstein G (2019) Scene Representation Networks: Continuous 3D-Structure-Aware Neural Scene Representations. In: 33rd Conference on Neural Information Processing Systems (NeurIPS 2019), pp. 1121 - 1132. Vancouver, Canada.

[7] Alatan AA, Yemez Y, Gudukbay U, Zabulis X, Muller K, Erdem CE, Weigel C, Smolic A (2007) Scene Representation Technologies for 3DTV-A Survey. IEEE Transactions on Circuits and Systems for Video Technology 11:1587-1605. https://doi.org/10.1109/TCSVT.2007.909974

[8] Mildenhall Ben, Srinivasan PP, Tancik M, Barron JT, Ramamoorthi R, Ng R (2021) NeRF: representing scenes as neural radiance fields for view synthesis Commun. ACM 1:99-106. https://doi.org/10.1145/3503250

[9] Kerbl B, Kopanas G, Leimkuehler T, Drettakis G (2023) 3D Gaussian Splatting for Real-Time Radiance Field Rendering. ACM Trans. Graph. 42(4), Article n. 139, pp. 1 - 14. https://doi.org/10.1145/3592433

[10] Brooks CR, Choudhury A (2002) Failure analysis of engineering materials. The McGraw-Hill Education. 1st edn. New York, NY.

[11] Sause MGR, Jasiūnienė E (2022) Structural Health Monitoring Damage Detection Systems for Aerospace. Springer Aerospace Technology. 1st edn. Cham, Switzerland. https://doi.org/10.1007/978-3-030-72192-3_11

[12] Trombini M, Maculotti G, Maisano DA, Pagani A, Franceschini F (2025) Scaling photogrammetry: A comparative evaluation and metrological assessment across small- and meso-scale domains. Precision Engineering 92:124-140. https://doi.org/10.1016/j.precisioneng.2024.12.002

[13] Luhmann T, Robson S, Kyle S, Harley I (2006) Close range photogrammetry. 1st edn. Wiley Whittles Publishing Caithness, UK.

[14] Franceschini F, Galetto M, Genta G (2015) Multivariate control charts for monitoring internal camera parameters in digital photogrammetry for LSDM (Large-Scale Dimensional Metrology) applications. Precision Engineering 42:133-142. https://doi.org/10.1016/j.precisioneng.2015.04.008

[15] Findlay SJ, Harrison ND (2002) Why aircraft fail. Material Today 5(11):18-25. https://doi.org/10.1016/S1369-7021(02)01138-0

[16] Agisoft. Discover intelligent photogrammetry with Metashape. https://www.agisoft.com/ Last accessed 25 April 2025.

[17] Fischler MA, Bolles RC (1981) Random sample consensus: a paradigm for model fitting with applications to image analysis and automated cartography. Commun. ACM 24(6):381-395. https://doi.org/10.1145/358669.358692